APL Energy

RESEARCH ARTICLE | JANUARY 23 2024

Permanent-magnet-based transverse thermoelectric generator with high fill factor driven by anomalous Nernst effect

Fuyuki Ando ; Takamasa Hirai ; Ken-ichi Uchida

APL Energy 2, 016103 (2024)
https://doi.org/10.1063/5.0180506

Permanent-magnet-based transverse thermoelectric generator with high fill factor driven by anomalous Nernst effect

Cite as: APL Energy 2, 016103 (2024); doi: 10.1063/5.0180506
Submitted: 10 October 2023 • Accepted: 19 December 2023 •
Published Online: 23 January 2024

Fuyuki Ando,[a] Takamasa Hirai, and Ken-ichi Uchida[a]

AFFILIATIONS

National Institute for Materials Science, Tsukuba 305-0047, Japan

[a]Authors to whom correspondence should be addressed: ANDO.Fuyuki@nims.go.jp and UCHIDA.Kenichi@nims.go.jp

ABSTRACT

A transverse thermoelectric generator for magnetic-field-free and high-density power generation utilizing the anomalous Nernst effect is constructed and its performance is characterized. By alternately stacking two different permanent magnets with the large coercivity and anomalous Nernst coefficients of opposite sign, transverse thermoelectric voltage and power can be generated in the absence of external magnetic fields and enhanced owing to a thermopile structure without useless electrode layers. In the permanent-magnet-based stack, the magnetic attractive force enables easy construction of the thermopile structure with a high fill factor. In this study, we construct a bulk module consisting of 12 pairs of $SmCo_5$- and $Nd_2Fe_{14}B$-type permanent magnets having positive and negative anomalous Nernst coefficients, respectively, whose fill factor reaches ~80%, whereas that of conventional thermoelectric modules based on the Seebeck effect is typically 30%–60%. We demonstrate magnetic-field-free anomalous Nernst power generation up to 177 μW at a temperature difference of 75 K around room temperature, which corresponds to the largest anomalous Nernst power density of 65 $\mu W/cm^2$. The presented module structure concept will provide a design guideline for high-performance transverse thermoelectric power generation.

In the urgent issue of sustainable energy solutions, thermoelectric generation technology attracts much attention as a promising avenue for harvesting waste heat and converting it into electricity. The conventional thermoelectric generation is driven by the Seebeck effect, which induces an electric field **E** in the direction parallel to a temperature gradient ∇T. Thus, the Seebeck effect is classified into a longitudinal thermoelectric effect. Due to the parallel relationship between **E** and ∇T, a thermoelectric generator (TEG) based on the Seebeck effect needs to consist of many legs of *p*- and *n*-type semiconductors, which are arranged in isolation to prevent a short-circuit fault and connected with each other in series on the hot and cool sides by electrode materials to enhance the output power. Such a Π-shaped module configuration imposes two problems that reduce the output power. The first problem of the Π-shaped structure is that the temperature gradient and optimum current density in the thermoelectric materials respectively decrease due to the contact thermal and electrical resistances at the electrode junctions, which especially deteriorate faced on the hot side.[1–3] The second problem is caused by the low fill factor, which is the area density of the active thermoelectric materials within the module. As the fill factor decreases, the power density proportionally decreases, and a part of the input heat flow is wasted as radiation and convection heat losses.[4–6] The fill factor of conventional bulk TEGs based on the Seebeck effect is typically in the range of 30%–60%[5,7,8] and at most ~70%.[9] These two problems prevent efficient power generation, resulting in limited applications of the thermoelectric generation technology.

A key to overcome the first problem is a utilization of transverse thermoelectric effects, which generate an electric field **E** in the direction perpendicular to ∇T. Owing to the orthogonal relationship between **E** and ∇T, the electric circuit of transverse TEGs can form without junctions faced on the hot side and scale up simply by elongating the length of thermoelectric materials along **E** without increasing the number of junctions.[10–15] To utilize this geometrical advantage, many studies have recently focused on developing physics, materials science, and applications of transverse thermoelectric phenomena.[3] Among the various transverse thermoelectric phenomena, studies on the anomalous Nernst effect (ANE) have

rapidly progressed with the development of topological materials science and spin caloritronics.[16–22] As shown in Fig. 1(a), the ANE-driven electric field $\mathbf{E}_{ANE}$ is in the cross-product direction (y-axis) of ∇T (x-axis) and the spontaneous magnetization (z-axis) in a magnetic material as shown in the following equation:

$$\mathbf{E}_{ANE} = S_{ANE}(\mathbf{m} \times \nabla T), \quad (1)$$

where S_{ANE} is the anomalous Nernst coefficient and $\mathbf{m}$ is the unit vector of magnetization. Typical TEGs based on ANE or the ordinary Nernst effect have been proposed with the thermopile and coil geometries having the advantages of simplicity for electrical wiring and suppression of thermal deterioration at the electrode junctions.[10–13]

However, conventional transverse TEGs have other problems. The aforementioned second problem regarding the fill factor still remains in conventional transverse TEGs. A scalable Nernst device with the coil geometry has been recently demonstrated with a relatively high fill factor (~70%) by thinning the insulator layers.[13] Meanwhile, the fill factor of transverse TEG with thermopile geometry was still 26% because it requires adequate space to form a zigzag circuit by single thermoelectric materials and electrodes.[14] Therefore, an effective way to improve the fill factor in thermopile geometry needs to be established. Furthermore, ANE and the ordinary Nernst effect in many materials work only under external magnetic fields.[10,11,22,23] In the case of ANE, the elongation of magnetic materials along the y-axis increases the ANE-induced thermoelectric voltage, whereas $\mathbf{m}$ necessarily directs along the hard axis of shape magnetic anisotropy (z-axis) due to the orthogonal relationship between $\mathbf{E}_{ANE}$ and $\mathbf{m}$. To solve this issue, the use of permanent magnets such as $SmCo_5$- and $Nd_2Fe_{14}B$-type magnets has recently been proposed, which enables the magnetic-field-free operation of ANE owing to large coercivity and remanent magnetization.[23–25] However, the use of permanent magnets in thermopile geometry has not been demonstrated so far.

In this study, we present a concept of bulk transverse TEGs based on ANE to realize a high fill factor and magnetic-field-free operation simultaneously. Figures 1(a) and 1(b) show the schematics of the components and module structure for the proposed transverse TEG, respectively. Transverse TEG consists of two different and alternately stacked permanent magnets with positive and negative S_{ANE} intermediated by thin insulator layers. As a proof-of-concept demonstration, we fabricate permanent-magnet-based transverse TEG comprising many $SmCo_5$- and $Nd_2Fe_{14}B$-type permanent magnet slabs having positive and negative S_{ANE}, respectively.[23] The use of permanent magnets as components in the thermopile structure allows us to easily construct TEG with a fill factor of ~80%, which is much higher than the fill factors used in the literature.[13,14] All the $SmCo_5$ and $Nd_2Fe_{14}B$ slabs are confirmed to positively contribute to the total transverse thermoelectric output by the lock-in thermography (LIT) method.[23–28] An ANE-induced thermoelectric voltage is generated without an external magnetic field and its magnitude is ideally equal to the calculated one from S_{ANE} of $SmCo_5$ and $Nd_2Fe_{14}B$. As a result of its structural design, the maximum ANE-induced output power reaches 177 μW at a temperature difference of ΔT = 75 K, which corresponds to an ANE-induced power density of 65 $\mu W/cm^2$. This power density is the largest value among transverse TEGs based on ANE.[29]

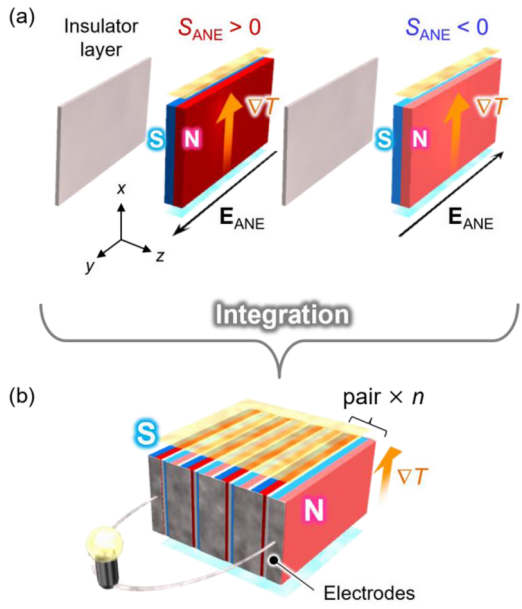

FIG. 1. Schematics of permanent magnets showing ANE and insulator layers (a) and integrated transverse TEG (b). The electric field induced by ANE $\mathbf{E}_{ANE}$ is generated in the cross-product direction (y-axis) of a temperature gradient ∇T (x-axis) and the spontaneous magnetization (z-axis) in a magnetic material. By alternately stacking two different permanent magnets with positive and negative anomalous Nernst coefficients S_{ANE} intermediated by insulator layers, a high-density module is obtained. n is the number of permanent magnet pairs. Electrodes are attached at the ends of the permanent magnets.

The important point of transverse TEG structure in Fig. 1(b) is to utilize not only positive and negative S_{ANE} values but also the magnetic attractive force due to the remanent magnetization of permanent magnets. The series circuit can be formed by inserting thin insulator layers between the neighboring magnets and electrically connecting the ends of magnets to sum up the transverse thermoelectric voltage in a zigzag manner. The circuit structure drastically increases the fill factor by reducing superfluous spaces for electrical wiring between the magnets. The magnetic attractive forces between permanent magnets allow the construction of a dense stack of themselves and stabilization of the remanent magnetization along the z-axis, owing to the stray field of neighboring magnets.

First, we investigated the thermoelectric and magnetic properties of the $SmCo_5$- and $Nd_2Fe_{14}B$-type permanent magnet slabs. We used $SmCo_5$ and $Nd_2Fe_{14}B$ circular disks with a thickness of 0.5 mm and diameter of 20 mm, having the easy axis of magnetic anisotropy along the thickness direction, which were commercially available from Magfine Corporation. The surface of $Nd_2Fe_{14}B$ disks was coated by a Ni–Cu–Ni plating layer with a thickness of ~15 μm to prevent oxidization.[30] To quantitatively estimate S_{ANE} of these magnets without applying an external magnetic field, we used the LIT method. The LIT method enables measurement of the anomalous Ettingshausen effect (AEE), the reciprocal effect of ANE, and the estimation of S_{ANE} through the Onsager reciprocal relation: $\Pi_{AEE} = S_{ANE}T$ with Π_{AEE} being the anomalous Ettingshausen coefficient. The experimental procedure to estimate Π_{AEE} is the same as that

used in previous reports.[23–28] Figure 2(a) shows the measurement results of S_{ANE} and Π_{AEE} at 300 K in the absence of external magnetic fields. The S_{ANE} values for $SmCo_5$ and $Nd_2Fe_{14}B$ in the remanent states were estimated to be $+3.5 \times 10^{-6}$ and -8.7×10^{-7} V/K, respectively, the magnitude and sign of which are consistent with those reported in Ref. 23. Figures 2(b) and 2(c), respectively, show the electrical conductivity σ measured by a four-probe method and the thermal conductivity κ estimated from thermal diffusivity measurements using a laser flash analyzer and differential scanning calorimetry. According to the obtained S_{ANE}, σ, and κ values, the transverse thermoelectric figure of merit $z_{ANE}T$ $(=S_{ANE}^2\sigma T/\kappa)$ for $SmCo_5$ and $Nd_2Fe_{14}B$ was estimated to be 4.2×10^{-4} and 2.5×10^{-5} at 300 K, respectively. Meanwhile, we measured the magnetization M curves for these magnets while applying an external magnetic field $\mathbf{H}$ along the thickness direction to confirm the remanent magnetization. Figure 2(d) shows the results of the M–H curves obtained at room temperature. Both the $SmCo_5$ and $Nd_2Fe_{14}B$ slabs show a remanent magnetization comparable to the saturation magnetization and a large coercivity, enabling the magnetic-field-free operation of ANE.

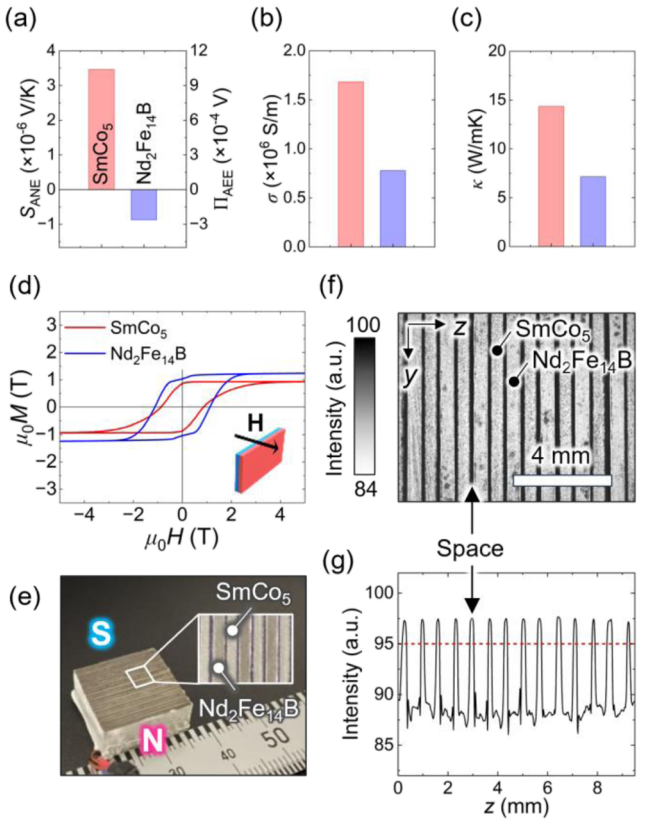

FIG. 2. Measurement results of the anomalous Nernst coefficient S_{ANE} (a), electrical conductivity σ (b), thermal conductivity κ (c), and magnetization M curves (d) for the $SmCo_5$- and $Nd_2Fe_{14}B$-type permanent magnets, where μ_0 is the magnetic permeability of vacuum. (e) Photograph of transverse TEG composed of 12 pairs of $SmCo_5$ and $Nd_2Fe_{14}B$ slabs. The inset shows the TEG's top surface. (f) The infrared image of the top surface. (g) Line profile of the infrared intensity along z-axis.

The next step is to fabricate high-density TEG using pairs of $SmCo_5$ and $Nd_2Fe_{14}B$ slabs. Figure 2(e) shows the photograph of our transverse TEG consisting of 12 alternately stacked $SmCo_5/Nd_2Fe_{14}B$ pairs. We inserted ~0.05-mm-thick paper towel layers soaked with heat-resistant glue (Aron Alpha Tough-power) between the slabs to avoid reduction of the ANE voltage due to shunting effects. After the glue cured, we cut the stacked disks into a rectangular shape with a size of 8.2 mm ($\|\nabla T$) × 16.5 mm ($\|\mathbf{E}$) × 16.5 mm ($\|$ the stacking direction) so that the $Nd_2Fe_{14}B$ surfaces were exposed on the planes attaching to electrodes and heat source/sink by removal of the Ni–Cu–Ni plating layers. The ends of neighboring $SmCo_5$ and $Nd_2Fe_{14}B$ slabs were manually and carefully connected by attaching indium to form a zigzag series circuit without short-circuit fault. Then, the stacked $SmCo_5$ and $Nd_2Fe_{14}B$ slabs were magnetized by applying a pulse magnetic field of +8 T in the stacking direction. The adhesion of slabs is reinforced by their magnetic attractive force. In this structure, the ANE voltage in all the slabs positively contributes to the total voltage owing to the positive (negative) S_{ANE} of $SmCo_5$ ($Nd_2Fe_{14}B$) when the ∇T and $\mathbf{m}$ directions in all the slabs are the same. The inset of Fig. 2(e) shows a top view of TEG, which confirms that the slabs are stacked with high density and separated by thin insulator layers.

To characterize the fill factor, we observed the infrared image of the top surface of $SmCo_5/Nd_2Fe_{14}B$-based TEG [Fig. 2(f)]. The fill factor can be estimated from the contrast of thermally emitted infrared intensity due to the difference in infrared emissivity between the metallic surfaces with low emissivity and paper towels with high emissivity. Here, the line profiles are taken along the z-axis as shown in Fig. 2(g), where the infrared intensity at each z-position is averaged along the y-axis. The contrast of infrared intensity was clearly observed between the slabs and their spaces, and the relative area of the slabs was estimated to be 81%, when the threshold infrared intensity value is set to be 95 [Fig. 2(g)].

The contribution of transverse thermoelectric conversion in each slab and the absence of a short-circuit fault in $SmCo_5/Nd_2Fe_{14}B$-based TEG is confirmed through AEE measurements by the LIT technique. Figure 3(a) shows a schematic of the LIT measurement setup for TEG. To quantitatively estimate the surface temperature, we coated the top surface of TEG by an insulating black ink with high infrared emissivity (>0.94). The LIT measurements were performed while applying a square wave charge current $\mathbf{J}_c$ with amplitude J_c, frequency f, and zero-offset.[23–28] The application of $\mathbf{J}_c$ generates an AEE-induced heat flow $\mathbf{J}_{q,AEE}$ in the cross-product direction of $\mathbf{J}_c$ and $\mathbf{m}$ as[31]

$$\mathbf{j}_{q,AEE} = \Pi_{AEE}(\mathbf{j}_c \times \mathbf{m}), \tag{2}$$

where $\mathbf{j}_c$ and $\mathbf{j}_{q,AEE}$ denote the charge current density and AEE-induced heat flow density, respectivily. As a result of $\mathbf{J}_{q,AEE}$ generation, the temperature on the surfaces of these magnetic materials is modulated. By extracting the transient first-harmonic temperature modulation signals of the thermal images and transforming them into lock-in phase φ and amplitude A by Fourier analysis, the pure contribution of thermoelectric effects, such as AEE and the Peltier effect, can be visualized without contamination by Joule heating.[26,27] In magnetized permanent magnets, the AEE-induced temperature modulation free from the Peltier effect can be measured in the absence of an external magnetic field

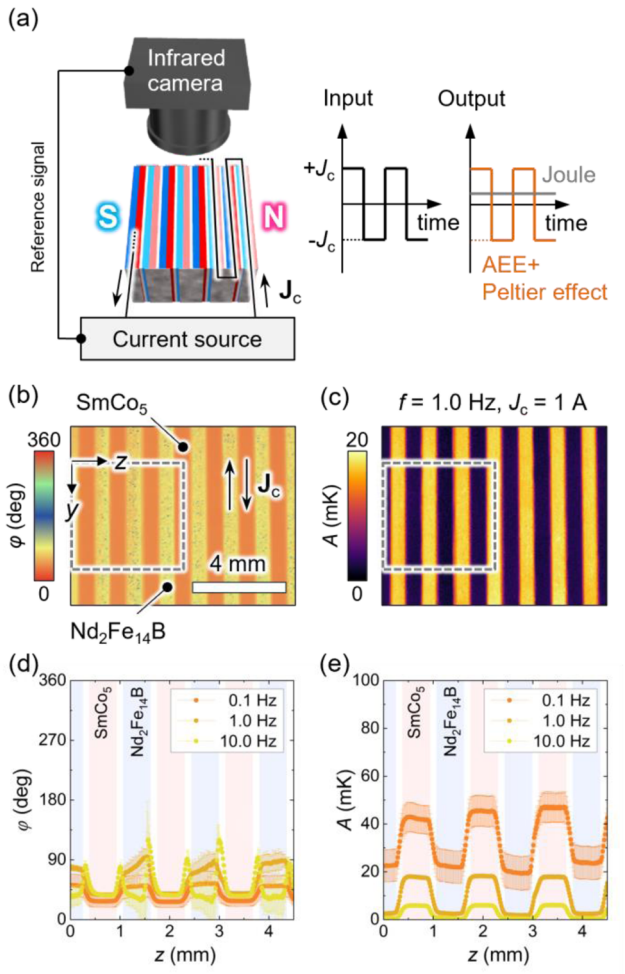

FIG. 3. (a) Schematic of the LIT measurement. Input charge current $\mathbf{J}_c$ flows in transverse TEG in a zigzag manner. The top surface's temporal thermal image is measured to visualize pure contributions of thermoelectric effects. The lock-in phase φ (b) and amplitude A (c) images at f = 1.0 Hz and J_c = 1 A. Line profiles of φ (d) and A (e) along z-axis in the dotted area of (b) and (c), respectively, for various values of f.

in areas far from the sample edges.[23] The spatial distribution of modulation allows us to confirm that all the $SmCo_5$ and $Nd_2Fe_{14}B$ slabs correctly operate without short-circuit faults. Figures 3(b) and 3(c) show examples of the φ and A images at f = 1.0 Hz and J_c = 1 A, respectively. The thermoelectric signals on the top surface of $SmCo_5/Nd_2Fe_{14}B$-based TEG were clearly observed with high area density. Importantly, the $SmCo_5$ and $Nd_2Fe_{14}B$ slabs show spatially homogeneous A signals, which is consistent with the feature of AEE with $\mathbf{m}$ along the z-axis [Fig. 3(c)]. This uniformity confirms that $\mathbf{J}_c$ flows in a zigzag way [indicated by black arrows in Fig. 3(b)] without short-circuit fault. Because of the opposite direction of $\mathbf{J}_c$ and opposite sign of Π_{AEE} between $SmCo_5$ and $Nd_2Fe_{14}B$, the resultant temperature modulation due to AEE shows the same sign in all the slabs, which was confirmed by the almost identical φ values observed on the whole area of the top surface [Fig. 3(b)]. As shown in Fig. 3(c), the $SmCo_5$ slabs show larger A signals than $Nd_2Fe_{14}B$ slabs due to larger Π_{AEE} [Fig. 2(a)]. Figures 3(d) and 3(e) show the line profiles of φ and A taken along the z-axis, where the signals are averaged along the y-axis, within the area indicated by a 4.5 mm square in Figs. 3(b) and 3(c), respectively. The $Nd_2Fe_{14}B$ slabs show a large φ delay and rapid drop in A as f increases, which can be explained by the fact that $Nd_2Fe_{14}B$ has lower κ than $SmCo_5$ [Fig. 2(c)].[27] Thus, LIT measurements reveal that all $SmCo_5$ and $Nd_2Fe_{14}B$ slabs positively contribute to transverse thermoelectric conversion without any short-circuit fault, while the superfluous space for electrical wiring between neighboring slabs is significantly reduced.

We are in a position to demonstrate magnetic-field-free transverse thermoelectric power generation in $SmCo_5/Nd_2Fe_{14}B$-based TEG. Figure 4(a) shows a schematic and photograph of the setup for four-terminal measurements of thermoelectric power, where TEG was sandwiched by a heater and heat sink. When TEG is used, the current source will be replaced to a load resistor so that one can obtain the output power without an external power supply. The heat sink's temperature was controlled by flowing coolant at 273 K. The actual ΔT inside TEG was estimated by measuring the thermal image of its side surface coated by black ink. The hot and cool side temperatures (T_h and T_c) are defined as the highest and lowest temperatures of the thermal image in TEG along the heat flow direction.

To investigate the pure contribution of the ANE-induced thermopower independent of the parasitic Seebeck-effect-induced thermopower, we measured the dependence of the open circuit voltage V_{oc} on the remanent magnetization direction. We repeatedly reversed the remanent magnetization between the $+z$ and $-z$ directions, represented by $+M$ and $-M$ states, by applying a pulse magnetic field of 8 T and measured V_{oc} as a function of ΔT in the absence of an external magnetic field for two cycles [Fig. 4(b)]. We found that the sign of $V_{oc}/\Delta T$ was reversed by reversing the magnetization direction as shown in the inset of Fig. 4(b), indicating that the V_{oc} signal originates from pure ANE free from the offset due to the Seebeck effect. We confirmed that the V_{oc} value is quantitatively consistent with the calculated value from S_{ANE} of $SmCo_5$ and $Nd_2Fe_{14}B$ [Fig. 2(a)] as shown in the following equation:

$$V_{oc} = \frac{nl\left[\tilde{S}_{ANE}(SmCo_5) - \tilde{S}_{ANE}(Nd_2Fe_{14}B)\right]\cdot \mathbf{m}}{h}\cdot \Delta T, \quad (3)$$

where n is the number $SmCo_5/Nd_2Fe_{14}B$ pairs, l the length of each slab along the $\mathbf{E}_{ANE}$ direction, h the height of each slab along the ∇T direction, and $\tilde{S}_{ANE}$ the averaged S_{ANE} value at temperatures ranging from T_c to T_h. Here, we approximated $\tilde{S}_{ANE}$ for $SmCo_5$ and $Nd_2Fe_{14}B$ using the S_{ANE} values at room temperature. Figure 4(b) shows good agreement between the measured and calculated V_{oc} values, which confirms the fact that the thermoelectric voltage in our TEG is due purely to ANE.

The magnetic-field-free operation of ANE-induced power generation was demonstrated by measuring the thermoelectric voltage V by applying a load current I_{load} to TEG. Figure 4(c) shows the I_{load} dependence of the output power P at various values of ΔT, where P is the product of V and I_{load}. The high P, 177 μW at maximum when ΔT = 75 K and I_{load} = 41 mA, was obtained owing to both the

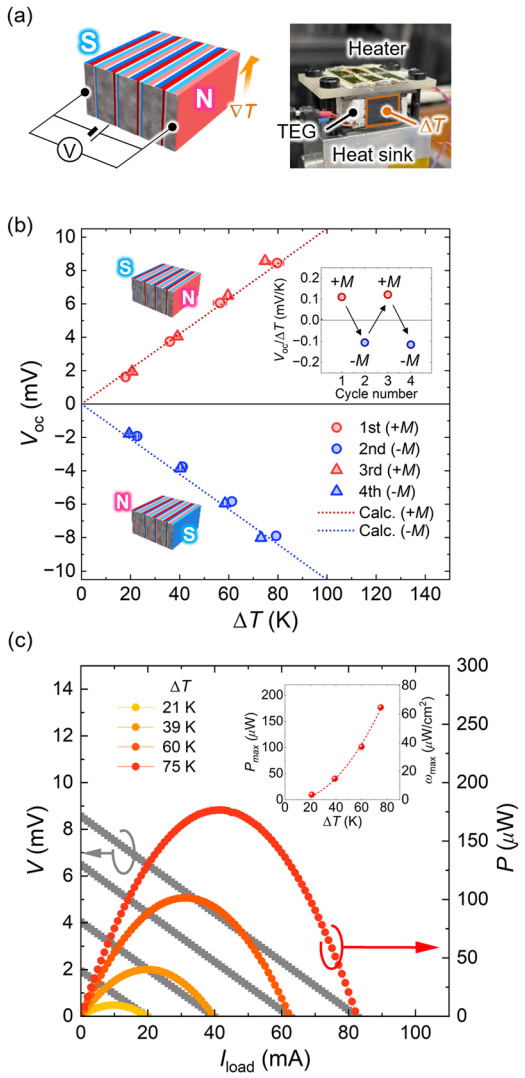

FIG. 4. (a) Schematic and photograph of transverse TEG to show the setup for four-terminal measurements of thermoelectric power and the area for estimating the temperature difference ΔT by a thermography. (b) ΔT dependence of the open circuit voltage V_{oc} when the remanent magnetization is along the $+z$ direction ($+M$) and $-z$ direction ($-M$). (c) Load current I_{load} dependence of the thermoelectric voltage V and output power P in the $+M$ state at various values of ΔT. The inset shows ΔT dependences of the maximum output power P_{max} and power density per unit area ω_{max}.

large V_{oc} and small internal resistance of module R_{module}, which is the slope of the $I_{load}-V$ curve. The R_{module} of TEG was estimated to be 9.9 mΩ at ΔT = 21 K, whereas the value calculated from the σ values and dimensions of $SmCo_5$ and $Nd_2Fe_{14}B$ is 9.1 mΩ; the deviation of R_{module} from the calculated value due to the electrodes and junctions is only +8%. The inset of Fig. 4(c) shows the ΔT dependences of the maximum output power P_{max} and power density per unit area ω_{max}, which is proportional to the fill factor. Owing to the high P_{max} of 177 μW and high fill factor of ~80%, the resultant ω_{max} reaches 65 $\mu W/cm^2$ at ΔT = 75 K, which is the highest value among transverse TEGs based on ANE.[29]

Finally, we discuss future developments and applications of permanent-magnet-based transverse TEG. Since the fill factor of TEG is determined by the thickness ratio between magnetic materials and insulator layers, we can further increase the fill factor and ω_{max} by using thinner insulator layers. Although the demonstrated P_{max} of 177 μW can be used, for example, as stand-alone power supply for wireless sensor network systems, further improvement of $z_{ANE}T$ in permanent magnets is required for widespread thermoelectric applications. This is because commercial TEGs based on the Seebeck effect exhibit 70–80 mW/cm^2 at temperature differences of 60–70 K around room temperature,[32,33] which are still three orders of magnitude larger than that of the presented transverse TEG based on ANE. Decreasing κ and increasing S_{ANE} in permanent magnets are the significant tasks, especially for those with negative S_{ANE}, since the small negative S_{ANE} of $Nd_2Fe_{14}B$ is a bottleneck in the output of our TEG. Additionally, the thermal durability of TEG is limited by that of the remanent magnetization in $Nd_2Fe_{14}B$-type permanent magnets, which gradually decreases beyond ~400 K.[34] Meanwhile, since the remanent magnetization of $SmCo_5$- and $Nd_2Fe_{14}B$-type permanent magnets around room temperature is at the highest level, our TEG enables energy harvesting from everywhere permanent magnets are used.

In conclusion, we constructed ANE-based transverse TEG with high fill factor and demonstrated its magnetic-field-free operation. As a proof-of-concept demonstration, we used $SmCo_5$- and $Nd_2Fe_{14}B$-type permanent magnets with large coercivity, large remanent magnetization, and S_{ANE} of opposite sign. The pairs of $SmCo_5$ and $Nd_2Fe_{14}B$ slabs were integrated into high-density TEG, whose fill factor surprisingly reaches ~80%. Using the LIT method, all the $SmCo_5$ and $Nd_2Fe_{14}B$ slabs were confirmed to positively contribute to transverse thermoelectric conversion without any short-circuit fault. An ANE-induced output power of 177 μW was generated at a temperature difference of 75 K without external magnetic field, which corresponds to the largest power density of 65 $\mu W/cm^2$ among TEGs based on ANE. This study manifests the importance of developing permanent magnet materials with large positive and negative S_{ANE} values together with large remanent magnetization. The device architecture proposed here will serve as a design guideline for high-performance transverse thermoelectric power generation.

The authors thank H. Sepehri-Amin and Y. Sakuraba for valuable discussions and K. Suzuki and M. Isomura for technical supports. This work was supported by ERATO "Magnetic Thermal Management Materials" (No. JPMJER2201) from JST, Japan, and NEC Corporation.

AUTHOR DECLARATIONS

Conflict of Interest

The authors have no conflicts to disclose.

Author Contributions

Fuyuki Ando: Data curation (lead); Formal analysis (lead); Investigation (lead); Methodology (equal); Validation (equal);

Writing – original draft (lead); Writing – review & editing (equal). **Takamasa Hirai**: Data curation (supporting); Investigation (supporting); Writing – review & editing (supporting). **Ken-ichi Uchida**: Conceptualization (lead); Funding acquisition (lead); Investigation (equal); Methodology (equal); Project administration (lead); Supervision (lead); Validation (equal); Writing – review & editing (lead).

DATA AVAILABILITY

The data that support the findings of this study are openly available in Zenodo at https://doi.org/10.5281/zenodo.10005678.[35]

REFERENCES

[1] G. Min and D. M. Rowe, J. Power Sources **38**, 253–259 (1992).
[2] S. Shittu, G. Li, X. Zhao, and X. Ma, Appl. Energy **268**, 115075 (2020).
[3] K. Uchida and J. P. Heremans, Joule **6**, 2240–2245 (2022).
[4] M. Gomez, R. Reid, B. Ohara, and H. Lee, J. Appl. Phys. **113**, 174908 (2013).
[5] P. Ying, H. Reith, K. Nielsch, and R. He, Small **18**, 2201183 (2022).
[6] F. Tohidi, S. Ghazanfari Holagh, and A. Chitsaz, Appl. Therm. Eng. **201**, 117793 (2022).
[7] Z. Bu, X. Zhang, Y. Hu, Z. Chen, S. Lin, W. Li, and Y. Pei, Energy Environ. Sci. **14**, 6506–6513 (2021).
[8] C. Xu, Z. Liang, W. Ren, S. Song, F. Zhang, and Z. Ren, Adv. Energy Mater. **12**, 2202392 (2022).
[9] F. Ando, H. Tamaki, Y. Matsumura, T. Urata, T. Kawabe, R. Yamamura, Y. Kaneko, R. Funahashi, and T. Kanno, Mater. Today Phys. **36**, 101156 (2023).
[10] M. H. Norwood, J. Appl. Phys. **34**, 594–599 (1963).
[11] Y. Sakuraba, Scr. Mater. **111**, 29–32 (2016).
[12] M. Ikhlas, T. Tomita, T. Koretsune, M. T. Suzuki, D. Nishio-Hamane, R. Arita, Y. Otani, and S. Nakatsuji, Nat. Phys. **13**, 1085–1090 (2017).
[13] Z. Yang, E. A. Codecido, J. Marquez, Y. Zheng, J. P. Heremans, and R. C. Myers, AIP Adv. **7**, 095017 (2017).
[14] M. Murata, K. Nagase, K. Aoyama, A. Yamamoto, and Y. Sakuraba, iScience **24**, 101967 (2021).
[15] M. R. Scudder, B. He, Y. Wang, A. Rai, D. G. Cahill, W. Windl, J. P. Heremans, and J. E. Goldberger, Energy Environ. Sci. **14**, 4009–4017 (2021).
[16] K. Uchida, H. Adachi, T. Kikkawa, A. Kirihara, M. Ishida, S. Yorozu, S. Maekawa, and E. Saitoh, Proc. IEEE **104**, 1946–1973 (2016).
[17] S. R. Boona, K. Vandaele, I. N. Boona, D. W. McComb, and J. P. Heremans, Nat. Commun. **7**, 13714 (2016).
[18] A. Sakai, Y. P. Mizuta, A. A. Nugroho, R. Sihombing, T. Koretsune, M. T. Suzuki, N. Takemori, R. Ishii, D. Nishio-Hamane, R. Arita, P. Goswami, and S. Nakatsuji, Nat. Phys. **14**, 1119–1124 (2018).
[19] H. Reichlova, R. Schlitz, S. Beckert, P. Swekis, A. Markou, Y. C. Chen, D. Kriegner, S. Fabretti, G. Hyeon Park, A. Niemann, S. Sudheendra, A. Thomas, K. Nielsch, C. Felser, and S. T. B. Goennenwein, Appl. Phys. Lett. **113**, 212405 (2018).
[20] W. Zhou, K. Yamamoto, A. Miura, R. Iguchi, Y. Miura, K. Uchida, and Y. Sakuraba, Nat. Mater. **20**, 463–467 (2021).
[21] K. Uchida, W. Zhou, and Y. Sakuraba, Appl. Phys. Lett. **118**, 140504 (2021).
[22] A. Von Ettingshausen and W. Nernst, Ann. Phys. **265**, 343 (1886).
[23] A. Miura, H. Sepehri-Amin, K. Masuda, H. Tsuchiura, Y. Miura, R. Iguchi, Y. Sakuraba, J. Shiomi, K. Hono, and K. Uchida, Appl. Phys. Lett. **115**, 222403 (2019).
[24] A. Miura, K. Masuda, T. Hirai, R. Iguchi, T. Seki, Y. Miura, H. Tsuchiura, K. Takanashi, and K. Uchida, Appl. Phys. Lett. **117**, 082408 (2020).
[25] R. Modak, Y. Sakuraba, T. Hirai, T. Yagi, H. Sepehri-Amin, W. Zhou, H. Masuda, T. Seki, K. Takanashi, T. Ohkubo, and K. Uchida, Sci. Technol. Adv. Mater. **23**, 767–782 (2022).
[26] T. Seki, R. Iguchi, K. Takanashi, and K. Uchida, Appl. Phys. Lett. **112**, 152403 (2018).
[27] R. Das, R. Iguchi, and K. Uchida, Phys. Rev. Appl. **11**, 034022 (2019).
[28] K. Uchida, S. Daimon, R. Iguchi, and E. Saitoh, Nature **558**, 95–99 (2018).
[29] G. Lopez-Polin, H. Aramberri, J. Marques-Marchan, B. I. Weintrub, K. I. Bolotin, J. I. Cerdá, and A. Asenjo, ACS Appl. Energy Mater. **5**, 11835–11843 (2022).
[30] K. Uchida, T. Hirai, F. Ando, and H. Sepehri-Amin, "Hybrid transverse magneto-thermoelectric cooling in artificially tilted multilayers," Adv. Energy Mater. 2302375 (published online).
[31] T. Seki, R. Iguchi, K. Takanashi, and K. Uchida, J. Phys. D: Appl. Phys. **51**, 254001 (2018).
[32] KELK Ltd., Products information on thermo generation module, see https://www.kelk.co.jp/english/generation/index.html
[33] Coherent Corp., Thermoelectric generator (TEG) modules, see https://ii-vi.com/product/thermoelectric-generator-teg-modules/
[34] D. Brown, B.-M. Ma, and Z. Chen, J. Magn. Magn. Mater. **248**, 432–440 (2002).
[35] F. Ando, Zenodo (2023) https://doi.org/10.5281/zenodo.